Hard Carbon Composite Electrodes for Sodium-Ion Batteries with Nano-Zeolite and Carbon Black Additives

Daniela Ledwoch,[a] James B. Robinson,[a] Dominika Gastol,[b] Katherine Smith,[c] Paul R. Shearing,[a] Daniel J. L. Brett,[a] and Emma Kendrick*[a, b]

To enable fast charging of sodium-ion batteries and eliminate metallic dendrite growth on the electrodes an improvement in electrode design is required. In this work, we show the benefit of a mixed composite electrode containing ionic and electronic conducting additives for a sodium-ion battery negative electrode. Hard carbon electrodes with 5% additive containing different proportions of zeolite and carbon black are coated. The performance of the electrodes is elucidated through electrochemical and physical characterization methods; fast sodiation, electrochemical impedance spectroscopy (EIS), galvanostatic intermittent titration techniques (GITT) and electron microscopy. The addition of zeolite improves the sodium-ion transport diffusivity within the composite electrode by an order of magnitude at low voltages and high states of charge. EIS shows significantly lower series and solid-electrolyte interphase (SEI) resistances in the zeolite containing electrode after cycling. The capacity retention at higher rates is improved and a significant reduction of sodium dendrite growth was observed after cycling. SEM images confirm that porosity is still present in the zeolite containing electrode samples, enabling a pore network for sodium ion transport. These results emphasize the importance and limitations of ionic transport within hard carbon electrodes, and the required optimisation between electronic and ionic conductivity for sodium ion transport in these electrodes.

1. Introduction

Recent advances in the electrification of transport, increased adoption of portable electronic devices, and the intention of many countries to switch to renewable energy production, have resulted in increased demand for energy storage, especially in batteries.[1–11] At present, lithium-ion batteries are ubiquitous; however, lithium is geographically concentrated in specific areas (predominately South America), with a global concentration of <70 ppm in the upper earth crust, which has led to discussions about its supply and sustainability.[12] As a result, alternatives, including Na-ion batteries, have been developed as a potential replacement for the Li-ion cell in specific applications. Besides other alternative technologies, including Li-air, Al-ion, and Mg-ion, the research and development on Na-ion cells is already proven technology and close to commercialization.[13–18] Similar to lithium-ion batteries, sodium-ion batteries often contain transition metal materials on the cathode side, e.g., layered oxide materials or phosphates, which are paired with a carbon-based negative electrode. Graphite cannot be reversibly cycled in sodium-ion batteries with carbonate electrolytes, so hard carbon is commonly used as the negative electrode material.[13,19–21] Compared to graphite, hard carbon has a lack of order in the c-direction, which causes a lower density but a higher 3-D electronic conductivity compared to graphite.[22] The effective diffusion coefficients for hard carbon, show a significant change in magnitude over the full sodiation range.[20,23–28] At the $>50\%$ sodiation the diffusion coefficient is orders of magnitude lower than at low levels of sodiation, and this may indicate future problems in terms of faster charge capabilities. Currently hard carbon is the anode of choice for sodium-ion batteries, therefore improvements in the observed charge rate are required for many of the potential applications on the horizon for sodium-ion batteries such as power tools, e-mobility (e-bikes, electric vehicles) and stationary energy storage. During cycling, and especially during the initial formation cycles, an electronically insulating solid-electrolyte interphase (SEI) forms on the anode surface, which is observed as a first cycle loss, this interface can increase internal resistance and cause a subsequent drop in cell performance.[27,29–32] The growth of the SEI decreases the porosity of the composite electrode as the SEI grows into the available pore space. Hence, possible electrolyte reservoirs vanish, and pathways for sodium-ion diffusion are elongated or removed altogether. In a full cell NIB system the first cycle loss

[a] D. Ledwoch, Dr. J. B. Robinson, Prof. P. R. Shearing, Prof. D. J. L. Brett, Prof. E. Kendrick
Electrochemical Innovation Lab
Department of Chemical Engineering
University College London
London, WC1E 6BT; United Kingdom
[b] Dr. D. Gastol, Prof. E. Kendrick
School of Metallurgy and Materials
University of Birmingham
Edgbaston, Birmingham, B15 2TT, United Kingdom
E-mail: e.kendrick@bham.ac.uk
[c] K. Smith
Johnson Matthey Technology Centre
Reading, RG4 9NH; United Kingdom

on the hard carbon can be detrimental to the reversible capacity, however as shown in previous systems with an O3-type layered oxide, the loss on the cathode in the first cycle can be utilised to form the SEI with no additional cumulative capacity losses.[33] This is preferential to any pre-sodiation of the hard carbons.

In this study, composite electrodes were manufactured, adding a commercially available solid ionic conductivity additive (NanoH-ZSM-5 P91, ACS Materials) to the electrode slurry to retain ionic pathways and maintain the ionic conductivity of the electrode. Besides the enhanced ionic conductivity, faster ion transport might be beneficial to reduce dendrite formation at high sodiation rates. The dendritic growth at high sodiation rates is a safety concern as the metallic dendrites cause internal short circuits accompanied by exothermal reactions and gas generation from the electrolyte.[34–40]

The spherical ionic conductivity additive zeolite (Ze) is made of SiO_2 and Al_2O_3 in a molar ratio of 1:91.[41] A cage size of 5Å was chosen to channel the solvated sodium ions efficiently.[42–45] Zeolite-like materials have been used in lithium-ion batteries before as a solid electrolyte, to capture moisture, to enhance the wettability of the separator, or use of a silicon-zeolite compound for better cycling stability.[46–55] Some patents state the use of metal composites (metal oxide and metal-carbon alloyed), such as zeolite, within the electrode slurry for lithium-ion batteries.[56] Previous work has shown the benefit of nano-zeolite additives at low weight percentages in sodium-ion electrolytes.[57] The authors are not aware of any publications with an approach using zeolite within the electrode slurry to enhance or maintain the ionic conductivity within the dried composite electrode structure for sodium-ion batteries to date.

This work compares the modified zeolite containing composite electrodes to standard electrodes to evaluate the influence of the additive within the electrode structure on the electrode performance. Galvanostatic intermittent titration technique (GITT) and desodation tests up to a rate of 5 C are conducted to determine ionic diffusion and rate performance of the electrodes.

2. Results and Discussion

Three composite electrodes are characterized and compared regarding their sodium-ion diffusion rate performance in the fresh and cycled state. Electrochemical characterization is carried out using GITT and rate tests and correlated with physical characteristics such as pore space and surface film formation. Postmortem analysis was performed using scanning electron microscopy (SEM) and energy-dispersive X-ray spectroscopy (EDS).

2.1. Electrochemical Characterization

Three electrodes were made with varying compositions of electronic and ionic conductivity additive, zeolite. The physical and electrochemical characteristics of the electrodes are summarised in Table 1, and the first two cycles at 10 mA g^{-1} shown in Figure 1. The specific capacity and first cycle loss was similar for the standard electrode and electrode A (1% zeolite additive), whereas the specific capacity and first cycle loss were slightly lower for electrode B (4% zeolite additive). The addition of zeolite leads to an increase in the electrical sheet resistance of the electrode, (Table S1 in Supplementary Information).

Table 1. Summary of working electrode properties used for the electrochemical testing.

	A:B:C:Ze[a]	Electrode porosity	Electrode loading [g m^{-2}]	AM[b] [g m^{-2}]	FCL[c] [%]	Specific capacity [mAh g^{-1}]
Standard Electrode	90:5:5:0	35%	129	116	14.8(2)	272(2)
Electrode A	90:5:4:1	35%	134	120	14.5(1)	271(4)
Electrode B	90:5:1:4	35%	122	110	13.0(2)	254(1)

[a] A: active material; B: PVDF binder; C: carbon black; Ze: zeolite (Ze). [b] AM: active material. [c] FCL: first cycle loss.
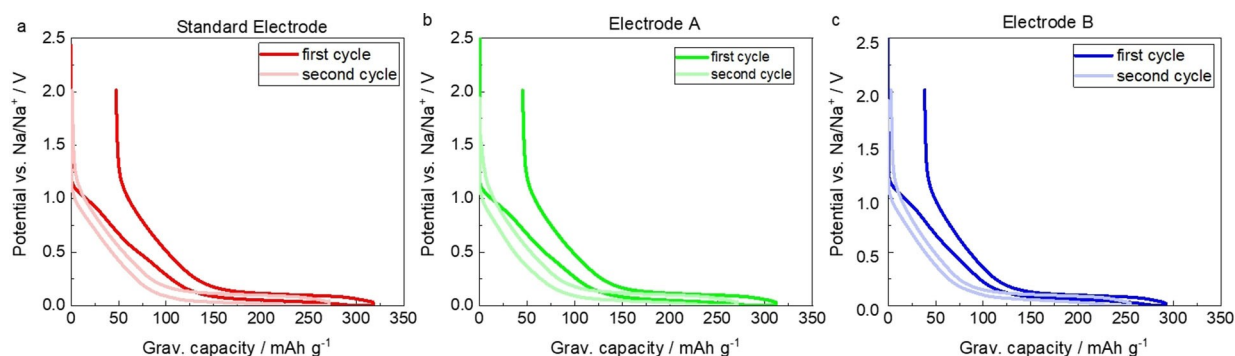
Figure 1. First and second cycle of hard carbon electrodes vs Na/Na$^+$ for a) standard electrode, b) electrode A with 4% CB and 1% Ze, and c) electrode B with 1% CB and 4% Ze.

Batteries & Supercaps

Articles
doi.org/10.1002/batt.202000161

Chemistry Europe
European Chemical
Societies Publishing

Further electrochemical testing parameters can be found in the Experimental section.

As shown in Figure 1, the first cycle loss is between 13 and 15%, with the reduction in carbon black additive the loss decreases. The higher first cycle loss is likely from the contribution of the carbon black to the electrode capacity, its high surface area and hence SEI formation on the conductive carbon additive as has been discussed previously.[58] The contribution of the carbon black to the observed specific capacity of the electrode is therefore negligible and at most 1.8% of the first cycle loss.
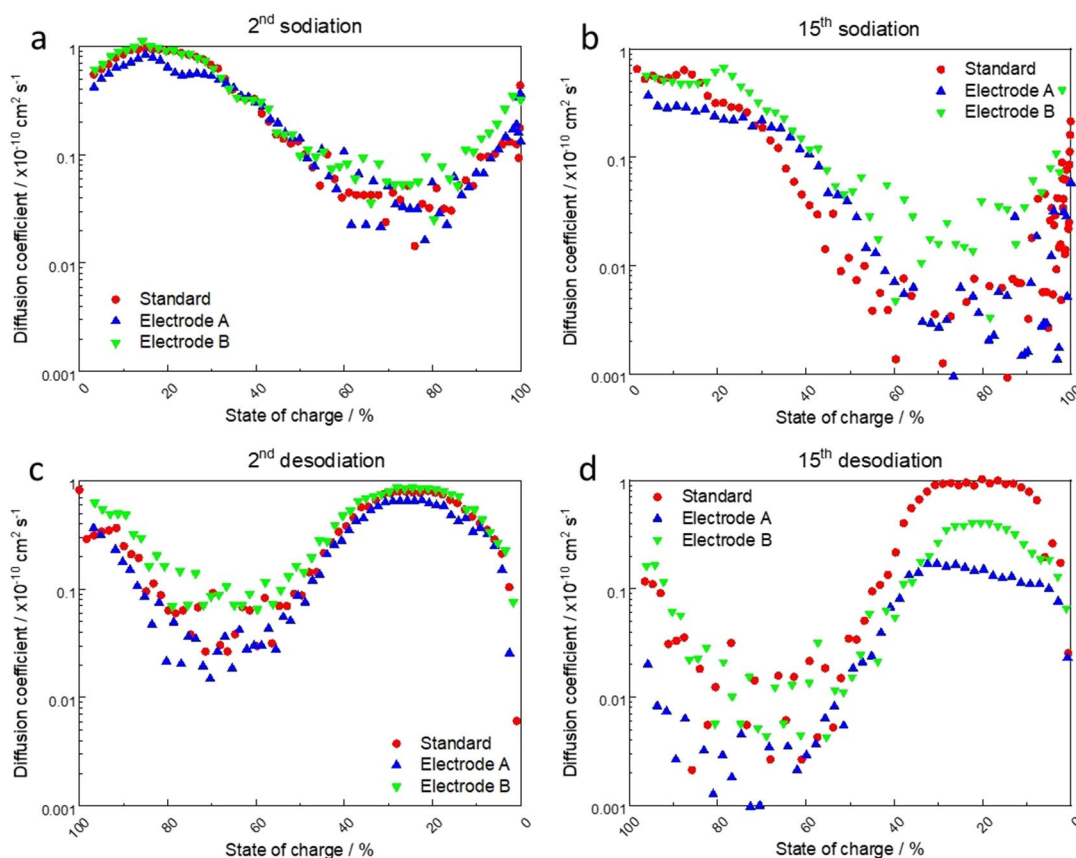
2.1.1. Apparent Diffusion Coefficients

GITT was performed to determine the apparent diffusion coefficients of sodium-ions within the electrode structure.[28,59–63] The resulting apparent diffusion coefficients ($\tilde{D}$, in cm^2 s^{-1}) were calculated using Equation (1)

$$\tilde{D} = \frac{4}{\pi\tau} \left(\frac{m_{AM} V_M}{M_{AM} S} \right)^2 \left(\frac{\Delta E_S}{\Delta E_t} \right)^2, \quad \left(\tau \gg \frac{L^2}{\tilde{D}} \right) \tag{1}$$

as introduced by Weppner and Huggins,[64] where τ is the applied current time interval ($\tau = 300$ s), m_{AM} is the electrode specific mass of active material (g), V_M is the molar volume (cm^3 mol^{-1}), M_{AM} is the atomic weight of the active material ($C_6 = 72$ g mol^{-1}), S is the active surface, L is the electrode thickness (cm), ΔE_S is the change in steady-state voltage per GITT step, and ΔE_t is the change in cell voltage per GITT step. ΔE_S and ΔE_t were obtained graphically, S was calculated from the electrode thickness, porosity and particle size (Table S2). Figure 2 shows the results of the diffusion behaviour for the 2nd and 15th cycle. The graphs display the effects of cycling upon the apparent diffusion coefficient. Figure 2 (a) and Figure 2 (b) show the values versus the capacity based on the 2nd cycle sodiation and desodiation, respectively. All electrodes show a similar behaviour following a wavelike profile; with a peak until around 100 mAh g^{-1} (approximately 20% state of charge (SoC)) with a maximum of 1×10^{-10} cm^2 s^{-1} followed by a trough until approximately 200 mAh g^{-1} (approximately 70% SoC) with a minimum of 1×10^{-12} cm^2 s^{-1}. The profile for desodiation features a similar trend in reverse, with smaller differences at the end of desodiation in terms of the length of the maximum plateau (175 mAh g^{-1} onwards). Figure 2 (c) and (d) display the apparent diffusion coefficients versus capacity based on the 15th cycle. The characteristic wavelike profile, as observed for the 2nd cycle, is maintained for this 15th cycle data for all electrodes during both sodiation and desodiation. However, the absolute values of the apparent diffusion coefficient values of all

Figure 2. Apparent diffusion coefficients versus the state of sodiation and desodiation, of one set of three different electrodes: standard electrode (5CB) (red circle), electrode A (1Ze:4CB) (blue triangle), and electrode B (4Ze:1CB) (green triangle). a) Profile during the second sodiation; b) profile during the second desodiation; c) profile during 15th sodiation; d) profile during 15th desodiation.

electrodes are decreased compared to those of the 2nd cycle. There are several key trends in this data:

- The diffusion coefficient between 0–50% SOC is several orders of magnitude higher than the 50–100% SOC.
- Samples which contain zeolite additive show higher apparent diffusion coefficients between 50–100% SOC than those without.
- The apparent diffusion coefficients for sodiation and desodiation are very similar for the 2nd cycle, but not for the 15th cycle.
- The diffusion coefficients for sodiation on the 15th cycle are slightly lower than that of the desodiation and between 50–100% SOC are higher with the zeolite additive than without.
- The desodiation shows significantly higher effective diffusion coefficients for the standard electrode than that containing zeolite additives.

These results indicate that the zeolite additive has a positive effect upon the low plateau sodiation, which is close to 0 V vs Na/Na$^+$, but has a negative effect upon desodiation at the low states of charge 50–0%. Table 2 lists the maximum and

minimum apparent diffusion coefficient values for the 2nd and 15th sodiation and desodiation.

Apparent diffusion coefficients of the sodium-ions within hard carbon based on GITT measurements have been published in the literature.[20,23–28] However, most of the published data is from uncycled electrodes and does not take the composite electrode features such as porosity and composition into account.[65–67] The pores within the electrode function as a reservoir of the highly ionic conductive electrolyte. Hence, the porosity, and the growth of the solid electrolyte interphase layer influences ionic mobility at the macroscale. In this study the porosities of the as-made electrodes are kept identical. Consequently, the change in the electrode performance observed here is due to the additive, and its effect upon the change in the porosity during cycling. The electrochemical impedance spectroscopy measurements (EIS) are shown in Figure 3. These show the difference in the resistances of the three electrodes in the 1st cycle, 2nd cycle and after cycling. In all cases Electrode B shows a greater resistance initially. The resistance at 0.005 V vs Na/Na$^+$ and 1 V vs Na/Na$^+$ all increase

Table 2. Average values for the maximum (max) and minimum (min) of apparent diffusion coefficients for the 2nd and 15th sodiation and desodiation ×10^{-10} cm^2 s^{-1}.

	2nd cycle apparent diffusion coefficient ×10^{-10} cm^2 s^{-1}]				15th cycle apparent diffusion coefficient [×10^{-10} cm^2 s^{-1}]			
	Sodiation		Desodiation		Sodiation		Desodiation	
SOC [%]	15	70	25	70	15	70	25	70
Standard Electrode (5%CB)	1.0	0.028	0.81	0.033	0.58	0.0012	1.0	0.0050
Electrode A (4%CB:1%Ze)	0.83	0.028	0.65	0.015	0.26	0.0019	0.15	0.0015
Electrode B (1%CB:4%Ze)	0.96	0.052	0.86	0.067	0.47	0.0145	0.40	0.0072
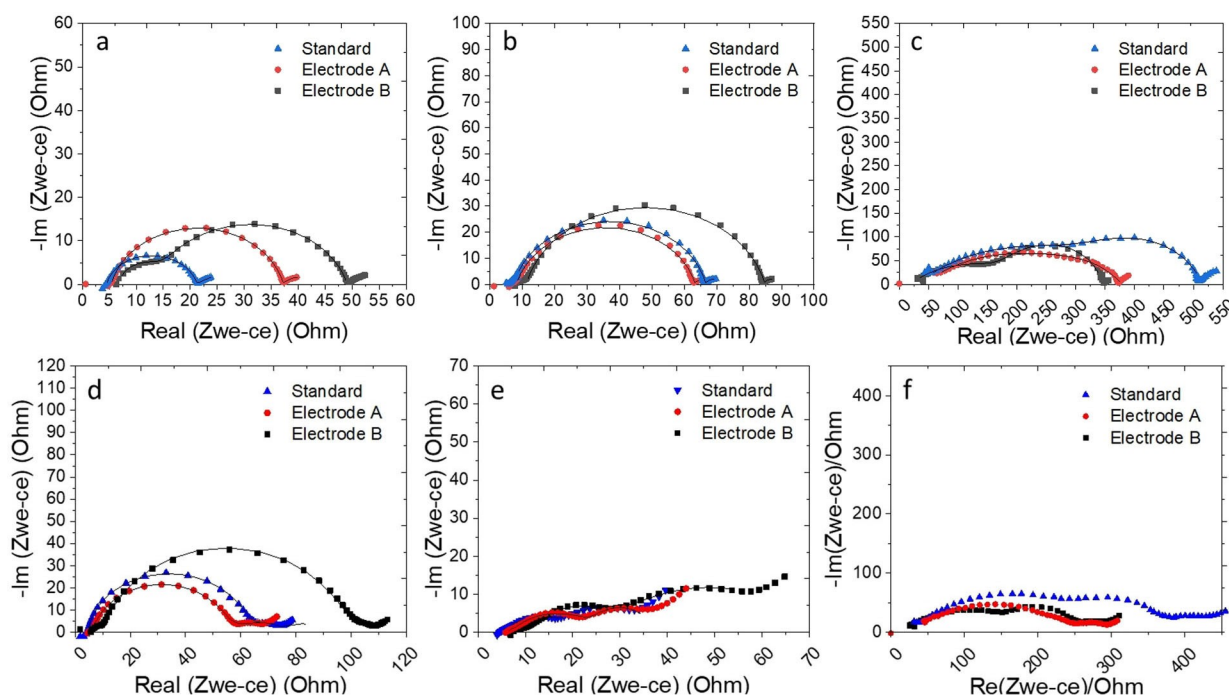
Figure 3. EIS for hard carbon composite electrodes; blue triangle (standard), red circles (electrode A), black squares (electrode B) and the equivalent circuit fits (black line) at 0.005 V vs Na/Na$^+$ for a) 1st discharge, b) 2nd discharge and c) after 10 cycles. At 1.0 V vs Na/Na$^+$ for d) 1st discharge, e) 2nd discharge and f) after cycling.

with cycling, however the Standard Electrode shows significant more resistance after cycling at 0 V vs Na/Na$^+$ compared to Electrode A and Electrode B. At 1 V vs Na/Na$^+$ the resistance of the Standard and Electrode A was very similar in the 1st and 2nd discharge, after cycling the resistance of the standard electrode was again significantly greater than either Electrode A or Electrode B. The series resistance of the cells also changed with cycling, and these are shown in Supplementary Table S3. The series resistance of the Standard Electrode and Electrode A both increase more than Electrode B.

The results of the GITT measurements indicate that the addition of an ionic conductivity additive effects the sodiation of the hard carbon at the low voltage region, between 50–100% state of charge. From the EIS results we can observe that in the low voltage region, the total charge transfer resistance after cycling of the standard electrode increases more than the electrodes with ionic additive; in the high voltage region the same is also true. The EIS at 0.005 V vs Na/Na$^+$ for the Standard and Electrode B was fitted using an equivalent circuit model (Table S3). As observed from Figure 3(f) after cycling the resistance from the SEI decreases with increasing zeolite content.

2.1.2. Rate Testing

Rate testing at different rates is conducted to understand the polarisation and capacity retention of electrodes containing ionic (zeolite) and electronic (carbon black) conductive addi-

tives. C rate is based upon rated capacity of 300 mAh g^{-1}. Figure 4 (a) shows the voltage profile for a standard hard carbon electrode at three different C-rates, ranging from 0.1 C (30 mA g^{-1}) to 5.0 C (1500 mA g^{-1}), measured in a 3-electrode cell. A 3-electrode electrochemical set-up (see Experimental) was used to ascertain the true polarisation increase on the working electrode rather than the combined working and counter electrodes.[61,68,69] The increase in rate causes an increase in polarisation on the working electrode, and therefore the average voltage upon desodiation increases. Hence, the cut-off voltage is triggered earlier, and the capacity obtained decreases. This issue is addressed with the use of a three-electrode setup as used here.

The rate tests with increasing desodiation rates were conducted after formation (two symmetrical cycles at 0.2 C). After each desodiation, the hard carbon working electrode (HC WE) was fully sodiated by applying a constant current constant voltage (CCCV) sodiation at 0.2 C. The desodiation or charging of the hard carbon (in a half cell) at 1 C is shown in Figure 4 (c), the higher voltage cut-offs are included here to show the noisy signal at the higher voltages. This noise is typically observed when sodium dendrites are formed and touch to form an instantaneous short circuit the heat produced subsequently destroys or melts the dendrite.[23,70,71] This phenomena is termed a 'soft short'[72–78] and is accompanied by large coulombic inefficiencies between the charge and discharge capacities. The graph shows that with zeolite in the electrode, less noise is observed. The electrode which contains 1% nano zeolite, shows less noise than the 4% nano zeolite, indicating that
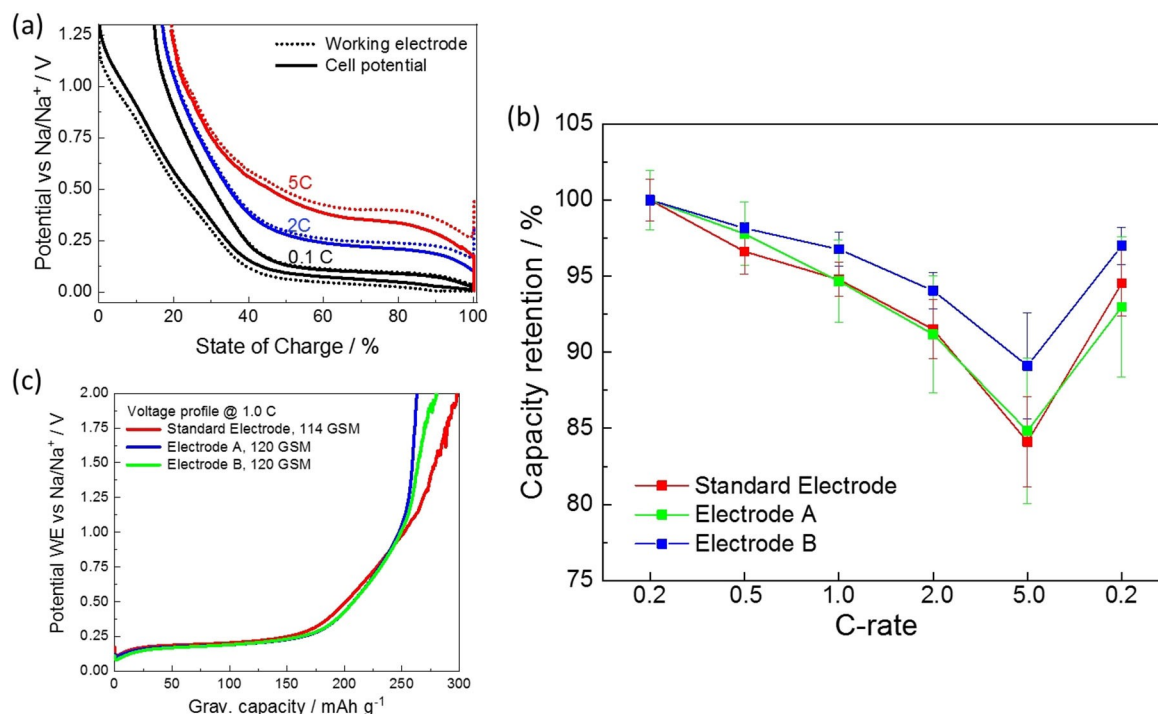
Figure 4. Performance graphs of rate testing. a) Profile of sodiation and desodiation profiles at different C-rates for cell (solid) and the working electrode (dotted) potential at 0.1, 2, and 5 C versus SoC for a standard electrode; b) Capacity retention for fast desodiation at different C-rates. Capacities are based on three test cells and measured via CCCV sodiation (5 mV, 0.01 C) at 0.2 C after each fast desodiation; c) desodiation voltage profiles at 1 C for a selection of three different composite electrodes versus capacity.

there is still a trade-off between electronic and ionic conductivity requirements in the electrode which require further optimisation. When these conductivities are optimised correctly this leads to less sodium plating. In order to evaluate the actual level of desodiation at these increasing rates, a low rate (0.2 C) constant current and constant voltage (CCCV) discharge (or sodiation) was performed, with a 5 mV and 0.01 C cut-off, the % capacity observed is shown in Figure 4 (b).

The observed initial capacities and first cycle losses are shown in the Supporting Information (Figure S1) and are similar to the data stated in the literature.[20] To account for aging effects, which are observed during cycling, the low C-rate of 0.2 C is repeated at the end of the fast charging tests to provide a comparative capacity. Compared to the third cycle at 0.2 C, the highest losses (around 8%) can be seen for Electrode B. The losses for the Standard Electrode are around 6%. In contrast, Electrode A has a total capacity loss of 4%.

A comparison of three voltage profiles of the 2nd and 8th sodiation is given in Figure 5. The addition of the ionic conductivity additive is accompanied by an increase in polarization, which can be seen in Figure 5 (a). The average voltage within the plateau region is shifted to lower potentials, triggering the constant-voltage step at lower capacities (in-set). After the rate test, the voltage profile for all three cells has

changed (Figure 5 (b)). Capacity losses are noticeable within the low plateau region, resulting in a ratio change of sloping versus plateau voltage region. Moreover, the polarization within the voltage plateau region increases compared to the second sodiation. The effect is most pronounced for the Standard Electrode and shows a similar profile for Electrode A and Electrode. B. Polarization increases with cycling due to increases in internal resistance. A lower polarization enhances obtainable capacities, especially at higher rates.

The discharging capacities decrease with increasing discharge current for all tested electrodes. Also, a distinct decrease in capacity can be seen for the Standard Electrode when the rate is changed from 2 C to 5 C.

Table 3 lists the average desodiation capacities, as displayed in Figure 4 (c). The observed desodiation capacities at different rates of the Standard Electrode and Electrode A are similar, whereas the cells of Electrode B show a lower desodiation capacity. This is due to the increase in electrical sheet resistance (Table S1). A significant increase in electrical sheet resistance is observed when the ionic conductivity additive content is increased, or carbon black content is decreased. Also, direct current internal resistance (DCIR) measurements conducted during GITT measurements show an increase in resistance for Electrode B compared to the Standard
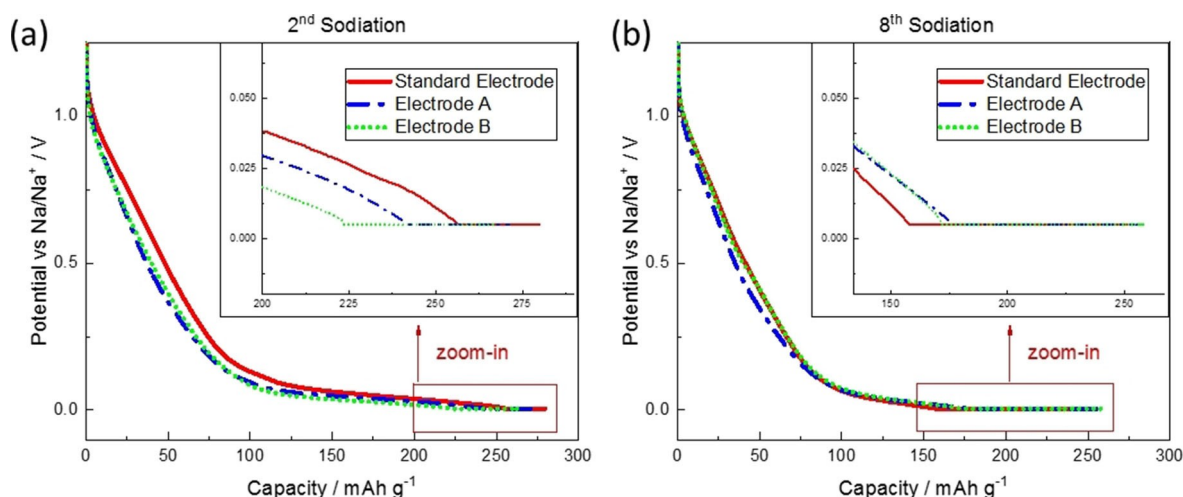

Figure 5. Sodiation profiles of the second a) and eighth b) sodiation for the standard electrode, electrode A, and electrode B.

Table 3. Average desodiation capacities based on three cells per set.[a]

| Cycle # C-rate	Standard (5%CB)		Electrode A (4%CB:1%Ze)		Electrode B (1%CB:4%Ze)	
	Capacity[b] [mAh g^{-1}]	percentage [%]	Capacity[b] [mAh g^{-1}]	percentage [%]	Capacity[b] [mAh g^{-1}]	percentage [%]
1st/0.2	303(3)	111	313(1)	116	301(8)	117
2nd/0.2	273(2)	100	270(2)	100	258(5)	100
3rd/0.2	271(4)	99	266(9)	99	255(5)	99
4th/0.5	262(4)	96	261(9)	97	250(5)	97
5th/1.0	257(3)	94	258(3)	96	242(7)	94
6th/2.0	248(5)	91	250(3)	93	233(10)	90
7th/5.0	228(8)	83	237(9)	88	217(7)	84
8th/0.2	256(6)	94	258(3)	96	237(11)	92

[a] Values are given in gravimetric capacities based on the hard carbon content. Percentage values are based on the second cycle capacities. Best performance values are highlighted. [b] Value in brackets represents the error.

Electrode (Figure S2). Electrode A shows the best capacity retention for all currents above 1 C as well as after the rate test, when examined at 0.2 C in both absolute and percentage values. The Standard Electrode and Electrode B show similar performance (excluding the first cycle loss), including a higher dependency on the current rate and higher overall losses (from the 2nd to the 8th cycle). We show in this work the effective diffusion coefficient and resistances of the electrodes. Long-term cycling is not possible in this 3-electrode configuration with a sodium metal anode and reference. As already observed sodium metal dendrites form very easily at the low voltages utilised in this work. In particular, with the significant polarisation of the sodium counter electrode especially at higher current densities, the formation of sodium metal dendrites is facilitated.[63,68]

2.2. Physical Characterization

The cycled electrodes were dismantled, and the physical and morphological changes investigated. Therefore, cycled electrodes are compared with fresh, as-made, electrodes. Photographs of two cycled electrodes (Standard Electrode and Electrode B) after cell dismantling can be found in the Supplementary Information (Figure S3). Sodium metal depositions are identified on both electrodes, showing higher amounts of deposition

on the Standard Electrode than on Electrode B. In Figure 6 SEM surface images of uncycled and cycled electrodes show a porous structure of large hard carbon particles (D_{50} particle size distribution as given by technical datasheet: 9 μm) and electrode additives. The uncycled Standard Electrode (Figure 6 (a)) shows large hard carbon particles embedded in a matrix of binder and carbon black where the edges and interspaces of the hard carbon particles can be seen to have a higher concentration of covering with carbon black. Figure 6 (b) shows an uncycled electrode B with 4% zeolite, the small cubic additives are the zeolite which are dispersed throughout the electrode along with the carbon black (small spherical particles). Most of the ionic conductivity additive "nests" in combination with the carbon black in the interspaces of the hard carbon particles. In these uncycled electrodes the edges of the hard carbon particles appear sharp, and the additives (binder, carbon black, ionic conductivity additive) can be distinguished from the hard carbon particle. In contrast, after cycling a film covers the hard carbon particles embedding the carbon black into its matrix (Figure S7). Features appear less distinct, and hard carbon particles less sharp. The cross sectional images of the Standard electrode and Electrode A are shown in Figure 6 (c and d). Where possible, the samples were transferred under inert conditions; however, contamination of the zeolite electrode samples and exposure to air limited any further analysis of Electrode B. The porosity of both electrodes
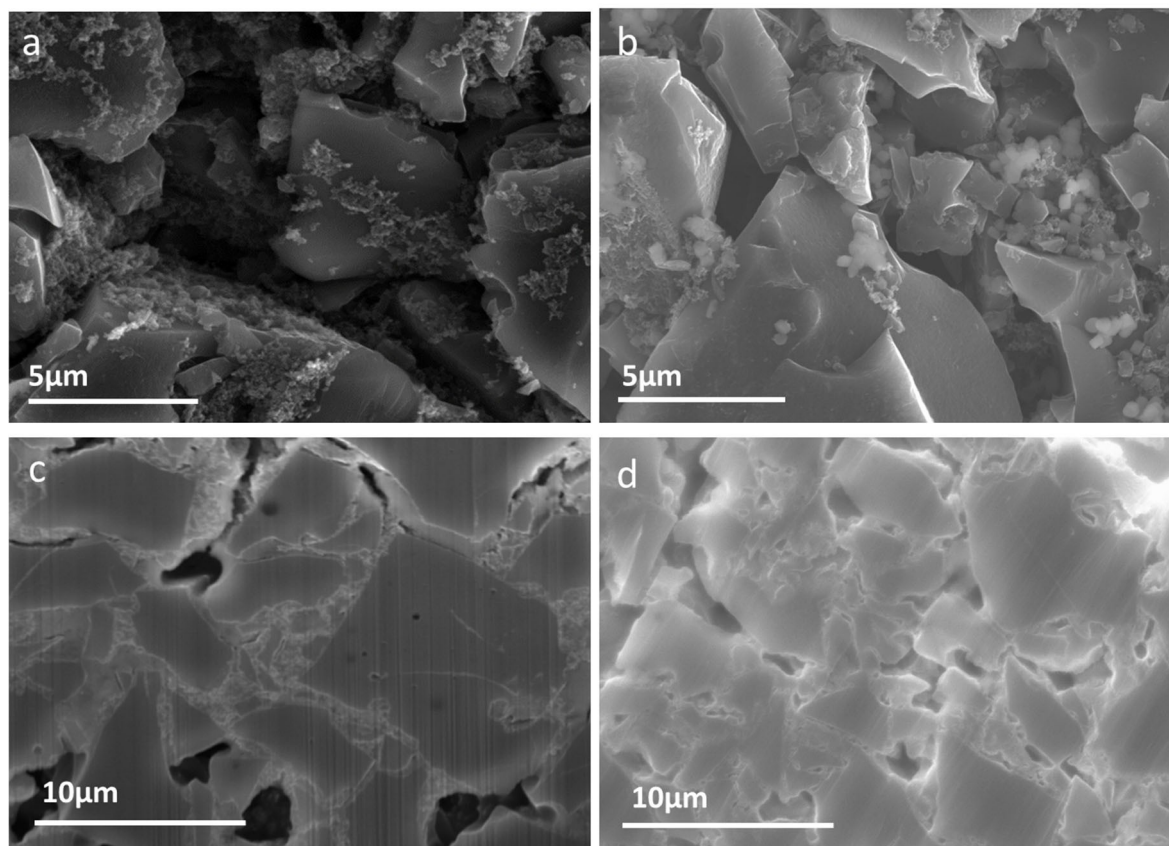
Figure 6. SEM images of an uncycled a) standard electrode and b) electrode B (4% Ze). Cross-sectional analysis of cycled electrodes c) standard electrode, d) electrode B detailed imaging of the particle network at 20k (lower row).

Batteries & Supercaps

Articles
doi.org/10.1002/batt.202000161

Chemistry Europe
European Chemical
Societies Publishing

are low, and an insulating layer which charged under the SEM, can be observed upon the surface of the hard carbon. In the Standard Electrode, there appears to be no small porosity between the hard carbon particles, this will cause problems for sodium ion transport between the particles, as there is no pore interconnectivity for the electrolyte transport. In the sample which contains the zeolite additive, an insulating surface covering is still apparent on the hard carbon, however the growth of the interface appears less than in the standard electrode, and small pores are observed. Further studies were performed upon the Standard Electrode in order to understand the reduction in apparent diffusion coefficient and the increase in resistance after cycling.

Cross-sections of Standard Electrodes (uncycled and cycled) were cut using a focused ion beam (FIB) to enable elemental mapping by EDS, (Figure S4, Table S4). The images show a cut area of approximately 15 μm depth and 30 μm width in the electrode structure. Again, the hard carbon particles of around 9 μm in size can be determined within the porous electrode structure. As the images are taken from cross-sections of a standard uncycled electrode, small encapsulated circular pores < 1 μm within the hard carbon material can be seen. The EDS image indicates an amount of carbon of 95 %, which is in accordance with the recipe composition (90 % hard carbon, 5 % carbon black). In the SEM image of the cycled Standard Electrode (Figure S4 (c)), the edges and surfaces of the hard carbon particles are brighter than the cut areas or compared to the uncycled electrode. The electronically insulating SEI accounts for the charging of the surface observed in the electron beam of the SEM. Based on these images, the porosity of the electrode is qualitatively observed to decrease. Additionally, brighter appearing material can be found in the interspace of the hard carbon particles. The EDS measurements show a composition of this material mainly based on sodium, but also shows oxygen, fluorine, and phosphorus from the decomposition of the electrolyte components (Figure S5 and Figure S6).[79] The images reveal the growth of the SEI into the empty pore space, reducing the porosity and blocking ionic and electronic pathways and subsequently reducing the conductivity within the electrode through cycling.

3. Conclusions

In this work, the effect of electrode formulations is investigated by partly substituting the electronic conductive additive carbon black with the ionic conductivity additive zeolite. A negative electrode with a coat weight 115($\pm$5) g m^{-2} and 35 % porosity was investigated where the electronically conductive carbon black was partly substituted with the ionically conducting zeolite. The ratio of additive to active material and binder content was kept constant (90:5:5, active:binder:additive). Electrochemical techniques; galvanostatic cycling, fast sodiation, EIS and GITT were used to determine the ionic conductivity, resistance, rate performance, and capacity retention of the composite electrodes. The physical characteristics such as porosity changes during cycling were investigated

using electron microscope imaging. The electrode composites which contain zeolite:carbon compositions (4:1) show improved rate performance (90 % at 5 C) and cycling stability where less sodium plating is observed. The effective diffusion coefficients extracted from the 15th cycle shows an order of magnitude increase upon the lower voltage plateaux (15 % SOC) from 1.5×10^{-12} cm^2 s^{-1} (4:1) compared to 1.2×10^{-13} cm^2 s^{-1} (0:5) during sodiation. Upon desodiation at higher states of charge (70 % SOC) within the sloping voltage region, the ionic conductivity is not the limiting factor and the effective diffusion appears decreased (0.4×10^{-10} cm^2 s^{-1} (4:1) 1×10^{-10} cm^2 s^{-1} (0:5)). This shows that changes in the ionic and electronic conductivity pathways during cycling is an important consideration when designing electrode microstructures. The physical characterization of the electrodes indicate that an interphase layer grows into the pores of the electrode microstructure during cycling, this correspondingly results in a reduction in electronic transport and an increase in Ohmic resistance and polarization. The growth of this interphase affects the porosity, 3-D electrode electronic and ionic conductivity due to the incorporation of the conductive carbon into the interphase reducing electronic transport properties. This also reduces sodium-ion transport pathways through vanishing electrolyte channels. The addition of a nano-zeolite additive in the electrode reduces the SEI on the hard carbon and helps keep open the sodium ion transport pathways. The ohmic resistance and the SEI resistance is reduced in these electrodes after cycling. Moreover, the zeolite additive helps to reduce sodium plating on the carbon surface at higher rates and upon cycling. This mixed ionic and electronic conductive approach for sodium-ion hard carbon electrodes enhances rate and improves aging characteristics, which may enable faster charging of sodium-ion batteries.

Experimental Section

Electrode manufacture

Three different composite electrodes were prepared. The Standard Electrode compromises a commercial HC material (D_{50} particle size distribution: 9 μm), polyvinylidene fluoride binder (PVdF, Kynar, HSV900), and carbon black (TimCal, C45) in a 90:5:5 wt.% ratio. Two sets of electrodes were made, replacing a part of the carbon black with a solid ionic conductivity additive (Nano-ZSM5 P91, ACS Material). Electrode A contains 90 % HC, 5 % binder, 4 % carbon black, and 1 % ionic conductivity additive. Electrode B contains 90 % HC, 5 % binder, 1 % carbon black, and 4 % ionic conductivity additive. N-methyl pyrrolidone (NMP) was used to formulate an ink aiming for a solid content of approx. 42 %. The ink was coated onto a carbon-coated aluminum current collector using the doctor blade method (MSK-AFA–L800BH, MTI). The electrodes were pre-dried using an infra-red lamp and then placed into a vacuum oven at 120 °C for at least 90 minutes to remove any NMP residues. All electrodes were calendered to a porosity of approximately 35 % by placing the electrode between two metal shims before feeding through the heated rollers of a calender machine (MTI Corporation, MSK-HRP-01, temperature: 90 °C). For porosity calculation, and active surface are of the electrode, the average density of the composite electrode materials and the volume of the dry coating

(electrode surface×thickness) were considered. Electrode thickness were measured with a micrometer gauge. Details are given in Table S1.

Cell building

12 mm electrode discs were cut from the prepared electrode sheets and transferred into a glove box (argon atmosphere). For cell building, a 3-electrode cell set-up was used utilizing a Tee-union compression fitting. An oil-free sodium ingot was flattened to approximately 0.5 mm thickness before 10 mm sodium discs were punched out as counter electrodes. An acceptor attachment of the 3-electrode cell was filled with sodium for reference electrode connection. A combination of one GF/A Whatman and one 20 μm polypropylene (PP) separator (2020, Celgard) were used in the cell stack and was placed perpendicular to the cell stack for electronic insulation of the reference electrode. A total of 130 μL of a premade electrolyte containing 1 M $NaPF_6$ in a 1:1 (v) mix of EC and DEC (Kishida Chemical Co. Ltd) was used as an electrolyte to wet both separator stacks.

Electrochemical characterization

Electrochemical testing was done using a BaSyTec potentiostat (CTS system, 1 μs time resolution., 0.05 μA current resolution, 0.3 mV voltage resolution), and EIS was performed on a Biologic VMP3. A full formation cycle at 0.2 C (based on an assumed capacity of 330 mAh g^{-1}) was conducted before testing. During formation, the cell was discharged in constant current/constant voltage (CCCV) mode, with a cut-off voltage of 0.005 V and a current of 0.01 C (sodiation process). Charging was conducted using a constant current (CC) at 0.2 C up to 2.0 V (desodiation process).

To perform the GITT measurements, a current equivalent to 0.2 C was applied for five minutes, followed by an open-circuit voltage (OCV) step with a termination condition based on a working electrode potential variation of $\triangle EWE \leq 0.001$ mV s^{-1}. The potential termination parameter is essential to ensure a quasi-equilibrium state of the electrode as ongoing diffusion processes and polarization affect the results.[68] Subsequent cycling was performed using identical parameters as for the formation cycle. For rate assessments, a set of three cells per electrode sheet was built and tested under the same conditions. These tests were performed after formation by varying the desodiation current from the third cycle onwards from 0.2 C to 0.5 C, 1.0 C, 2.0 C, 0.5 C, and back to 0.2 C while keeping the same sodiation conditions (CCCV sodiation at 0.2 C with a cut-off voltage of 5 mV). The EIS measurements using a BioLogic VMP3 system were conducted at 16 evenly spread potential steps within sodiation and desodiation, respectively. Each potential step was followed by a 150-minute OCV step to ensure full relaxation of the electrode to reach the equilibrium state before conducting the EIS measurement. For EIS a spectrum of 52 frequencies between 50 mHz and 1000 kHz were chosen, applying an amplitude of 2 mV and recording the average impedance based on three measurements per frequency. A low amplitude was chosen to minimize the contributions of SoC changes within the low plateau region. All electrochemical measurements were conducted at room temperature. Inks as being used for electrode preparations were made and coated using Mylar foil as substrate rather than a current collector foil. A four-point probe (linear array, Jandel cylindrical four point probe with HM21 hand held meter) was used to measure the in-plane conductivity of the coating. The probe was placed on different areas of the electrode sheet following a pattern from top to bottom and left to right, and an average value was written down. The pattern was kept identical for all electrodes. This enables us to neglect any contribution of the current collector and determine coating conductivity values only. A current was passed between the outer two probes, and the voltage difference measured between the two inner probes.

SEM and EDS measurements

For SEM and EDS imaging, an uncycled Standard Electrode (identical batch as used for electrochemical characterization) and a cycled Standard Electrode were used. The cell was cycled up to 47 cycles and charged to 1.75 V before being dismantled under inert atmosphere and transferred via an air-less transfer chamber to the SEM. An FEI **Scios** DualBeam system accessed at the Advanced Material Manufacturing Centre was used for all imaging.

A 1 μm thick layer of platinum was deposited on the surface to enable even material removal during FIB slicing. First, material in U-shape was removed to obtain a cuboid of material for conducting FIB slicing with an Auto Slice and View Software (Figure S8). The dimensions of the cuboid were set to 32×30×15 μm for the uncycled and 28×29×15 μm for the cycled sample, respectively. Next, slices with a thickness of 50 nm were removed using an ion beam current of 5 nA at an accelerating voltage of 30 kV. The resolution of the images taken was set to 1536×1024 pixels.

Conflict of Interest

The authors declare no conflict of interest.

[1] B. D. Farnsworth, J. Shipley, J. Lazar, N. Seidman, *Beneficial Electrification Ensuring Electrification in the Public Interest*, Montpelier, **2018**.
[2] U.S. EIA, *Annual Energy Outlook 2019 with Projections to 2050*, Washington, **2019**.
[3] Edison Electric Institute, *Transportation Electrification – Utility Fleets Leading the Charge*, Washington, **2014**.
[4] G. Meyer, R. Bucknall, D. Breuil, J. Affenzeller, L. Beaumel, *Electrification of the Transport System*, Brussels, **2017**.
[5] R. C. Stempel, *IEEE Electr. Insul. Mag.* **2005**, *18*, 38–42.
[6] M. Hilfer, L. Guerra, *"Boeing Autonomous Passenger Air Vehicle Completes First Flight"*, **2019**.
[7] S. Lekach, *Eng.* **2002**, *243*, 43.
[8] News CNRS, L. Cailloce [webpage on the Internet]. A battery Revolution in Motion. **2015**. Available from: https://news.cnrs.fr/articles/a-battery-revolution- in-motion. Accessed September 24, 2020.
[9] B. Fabiani Appavou, Adam Brown, D. Epp, B. Gibb, A. Kondev, E. McCrone, Hannah E. Murdock, L. Musolino, J. L. Ranalder, K. Sawin, J. Seyboth, F. S. Skeen, *Renewbles in Cities – 2019 Global Status Report*, Paris, **2019**.
[10] Climate Reality, "Follow the Leader: How 11 Countries Are Shifting to Renewable Energy," **2016**.

[11] P. B. Jones, J. Bosco, J. Howat, J. W. Van Alst, *The Future of Transportation Electrification: Utility, Industry and Consumer Perspectives*, **2018**.

[12] U. S. Geological Survey, *US Geol. Surv.* **2015**, 196.

[13] S. Roberts, E. Kendrick, *Nanotechnol. Sci. Appl.* **2018**, *11*, 23–33.

[14] K. Smith, J. Treacher, D. Ledwoch, P. Adamson, E. Kendrick, *ECS Trans.* **2017**, *75*, 13–24.

[15] K. Kubota, M. Dahbi, T. Hosaka, S. Kumakura, S. Komaba, *Chem. Rec.* **2018**, *18*, 459–479.

[16] A. M. Skundin, T. L. Kulova, A. B. Yaroslavtsev, *Russ. J. Electrochem.* **2018**, *54*, 113–152.

[17] SAS TIAMAT, **n.d.**

[18] HiNa Battery Technology Co., "Company Profile," **n.d.**

[19] B. Jache, J. O. Binder, T. Abe, P. Adelhelm, *Phys. Chem. Chem. Phys.* **2016**, *18*, 14299–14316.

[20] E. Irisarri, A. Ponrouch, M. R. Palacín, M. R. Palacin, *J. Electrochem. Soc.* **2015**, *162*, A2476–A2482.

[21] S. Komaba, W. Murata, T. Ishikawa, N. Yabuuchi, T. Ozeki, T. Nakayama, A. Ogata, K. Gotoh, K. Fujiwara, *Adv. Funct. Mater.* **2011**, *21*, 3859–3867.

[22] H. O. Pierson, *Handbook of Carbon, Graphite, Diamond and Fullerenes*, Noyes Publications, **1993**.

[23] C. Bommier, T. W. Surta, M. Dolgos, X. Ji, *Nano Lett.* **2015**, *15*, 5888–5892.

[24] Y. Li, Y.-S. Hu, M.-M. Titirici, L. Chen, X. Huang, *Adv. Energy Mater.* **2016**, *6*, 1600659.

[25] Q. Wang, X. Zhu, Y. Liu, Y. Fang, X. Zhou, J. Bao, *Carbon N. Y.* **2018**, *127*, 658–666.

[26] R. Väli, A. Jänes, T. Thomberg, E. Lust, *J. Electrochem. Soc.* **2016**, *163*, A1619–A1626.

[27] C. Bommier, D. Leonard, Z. Jian, W. F. Stickle, P. A. Greaney, X. Ji, *Adv. Mater. Interfaces* **2016**, *3*, 1600449.

[28] X. Li, X. Zeng, T. Ren, J. Zhao, Z. Zhu, S. Sun, Y. Zhang, *J. Alloys Compd.* **2019**, *787*, 229–238.

[29] P. Verma, P. Maire, P. Novák, *Electrochim. Acta* **2010**, *55*, 6332–6341.

[30] R. Mogensen, D. Brandell, R. Younesi, *ACS Energy Lett.* **2016**, *1*, 1173–1178.

[31] W. Zhang, M. Dahbi, S. Komaba, *Curr. Opin. Chem. Eng.* **2016**, *13*, 36–44.

[32] D. P. Finegan, M. Scheel, J. B. Robinson, B. Tjaden, I. Hunt, T. J. Mason, J. Millichamp, M. Di Michiel, G. J. Offer, G. Hinds, D. J. L. Brett, P. R. Shearing, *Nat. Commun.* **2015**, *6*, 6924.

[33] K. Smith, J. Treacher, D. Ledwoch, P. Adamson, E. Kendrick, *ECS Trans.* **2017**, *75*, 13–24.

[34] B. Lee, E. Paek, D. Mitlin, S. W. Lee, *Chem. Rev.* **2019**, *119*, 5416–5460.

[35] S. Liu, S. Tang, X. Zhang, A. Wang, Q. H. Yang, J. Luo, *Nano Lett.* **2017**, *17*, 5862–5868.

[36] Y. Zhao, K. R. Adair, X. Sun, *Energy Environ. Sci.* **2018**, *11*, 2673–2695.

[37] Y. Zhao, X. Yang, L.-Y. Kuo, P. Kaghazchi, Q. Sun, J. Liang, B. Wang, A. Lushington, R. Li, H. Zhang, X. Sun, *Small* **2018**, *14*, 1703717.

[38] X. Bi, X. Ren, Z. Huang, M. Yu, E. Kreidler, Y. Wu, *Chem. Commun.* **2015**, *51*, 7665–7668.

[39] A. Rudola, K. Saravanan, C. W. Mason, P. Balaya, *J. Mater. Chem. A* **2013**, *1*, 2653–2662.

[40] M. Jäckle, A. Groß, *J. Chem. Phys.* **2014**, *141*, 174710.

[41] ACS Material, "Technical Data Sheet: ACS Material Mesoporous Molecular Sieve Nano H-ZSM-5," **n.d.**

[42] M. T. Ong, O. Verners, E. W. Draeger, A. C. T. Van Duin, V. Lordi, J. E. Pask, *J. Phys. Chem. B* **2015**, *119*, 1535–1545.

[43] G. Åvall, *Modelling of Battery Electrolyte Interactions*, Chalmers University of Technology, **2018**.

[44] E. Flores, G. Åvall, S. Jeschke, P. Johansson, *Electrochim. Acta* **2017**, *233*, 134–141.

[45] C. N. Rowley, B. Roux, *J. Chem. Theory Comput.* **2012**, *8*, 3526–3535.

[46] C. Liang, *Separator and Electrolyte Material for Sodil Electroylte Battery Systems*, **1973**, *3*,736,186.

[47] V. Di Noto, S. Lavina, G. A. Giffin, E. Negro, B. Scrosati, *Electrochim. Acta* **2011**, *57*, 4–13.

[48] H. Saruwatari, T. Kishi, T. Kuboki, N. Takami, *Nonaqueous Electrolyte Battery*, **2006**, US 2003/0118900A1.

[49] S. Sanada, Y. Sekine, *Lithium Secondary Battery with a Laminate Housing Material*, **2008**, US20080206636A1.

[50] Y. Li, X. Wang, J. Liang, K. Wu, L. Xu, J. Wang, *Polymers (Basel).* **2020**, *12*, 764.

[51] J. Xu, X. Xiao, S. Zeng, M. Cai, M. W. Verbrugge, *ACS Appl. Mater. Interfaces* **2018**, *1*, 7237–7243.

[52] X. Dong, W. Mi, L. Yu, Y. Jin, Y. S. Lin, *Microporous Mesoporous Mater.* **2016**, *226*, 406–414.

[53] W. Xiao, Z. Gao, S. Wang, J. Liu, C. Yan, *Mater. Lett.* **2015**, *145*, 177–179.

[54] E. Shekarian, M. R. Jafari Nasr, T. Mohammadi, O. Bakhtiari, M. Javanbakht, *J. Appl. Polym. Sci.* **2019**, *136*, 47841.

[55] N. Kim, H. Park, N. Yoon, J. K. Lee, *ACS Nano* **2018**, *12*, 3853–3864.

[56] D. Ledwoch, E. Kendrick, P. Adamson, *Composite Electrode Including Microporous Ionically Conducting Material, Composite Slurry, and Methods of Manufacturing Same (Application)*, **2017**, US20180287134A1.

[57] L. Chen, B. Kishore, M. Walker, C. E. J. Dancer, E. Kendrick, *Chem. Commun.* **2020**, DOI 10.1039/D0CC03976D.

[58] R. Alcántara, J. M. Jiménez-Mateos, P. Lavela, J. L. Tirado, *Electrochem. Commun.* **2001**, *3*, 639–642.

[59] W. Weppner, R. A. Huggins, *J. Electrochem. Soc.* **1977**, *124*, 1569–1578.

[60] M. D. Levi, G. Salitra, B. Markovsky, H. Teller, D. Aurbach, U. Heider, L. Heider, *J. Electrochem. Soc.* **1999**, *146*, 1279.

[61] D. W. Dees, S. Kawauchi, D. P. Abraham, J. Prakash, *J. Power Sources* **2009**, *189*, 263–268.

[62] W. Zheng, M. Shui, J. Shu, S. Gao, D. Xu, L. Chen, L. Feng, Y. Ren, *Bull. Mater. Sci.* **2013**, *36*, 495–498.

[63] D. Ledwoch, D. J. L. L. Brett, P. R. Shearing, E. Kendrick, *ECS Trans.* **2017**, *75*, 81–90.

[64] W. Weppner, R. A. Huggins, *J. Solid State Chem.* **1977**, *22*, 297–308.

[65] J. Smekens, R. Gopalakrishnan, N. Van den Steen, N. Omar, O. Hegazy, A. Hubin, J. Van Mierlo, *Energies* **2016**, *9*, 1–12.

[66] G. Lenze, H. Bockholt, C. Schilcher, L. Froböse, D. Jansen, U. Krewer, A. Kwade, *J. Electrochem. Soc.* **2018**, *165*, A314–A322.

[67] R. Tian, S.-H. Park, P. J. King, G. Cunningham, J. Coelho, V. Nicolosi, J. N. Coleman, *Nat. Commun.* **2019**, *10*, 1933.

[68] D. Ledwoch, D. J. L. Brett, E. Kendrick, *ECS Trans.* **2016**, *72*, 17–22.

[69] Y. Zhu, T. Gao, X. Fan, F. Han, C. Wang, *Acc. Chem. Res.* **2017**, *50*, 1022–1031.

[70] D. A. Stevens, J. R. Dahn, *J. Electrochem. Soc.* **2000**, *147*, 1271.

[71] S. Alvin, D. Yoon, C. Chandra, H. S. Cahyadi, J. H. Park, W. Chang, K. Y. Chung, J. Kim, *Carbon N. Y.* **2019**, *145*, 67–81.

[72] W. Zhou, Y. Li, S. Xin, J. B. Goodenough, *ACS Cent. Sci.* **2017**, *3*, 52–57.

[73] R. Dugas, A. Ponrouch, G. Gachot, R. David, M. R. Palacin, J. M. Tarascon, *J. Electrochem. Soc.* **2016**, *163*, A2333–A2339.

[74] R. Rodriguez, K. E. Loeffler, S. S. Nathan, J. K. Sheavly, A. Dolocan, A. Heller, C. B. Mullins, *ACS Energy Lett.* **2017**, *2*, 2051–2057.

[75] S. Wei, S. Choudhury, J. Xu, P. Nath, Z. Tu, L. A. Archer, *Adv. Mater.* **2017**, *29*, 1605512.

[76] W. Luo, C.-F. Lin, O. Zhao, M. Noked, Y. Zhang, G. W. Rubloff, L. Hu, *Adv. Energy Mater.* **2017**, *7*, 1601526.

[77] Q. Wang, P. Ping, X. Zhao, G. Chu, J. Sun, C. Chen, *J. Power Sources* **2012**, *208*, 210–224.

[78] N. Zhao, C. Li, X. Guo, *Phys. Chem. Chem. Phys.* **2014**, *16*, 15646–15652.

[79] K. Li, J. Zhang, D. Lin, D.-W. Wang, B. Li, W. Lv, S. Sun, Y.-B. He, F. Kang, Q.-H. Yang, L. Zhou, T.-Y. Zhang, *Nat. Commun.* **2019**, *10*, 725.